Photoacoustics 34 (2023) 100572

Contents lists available at ScienceDirect

Photoacoustics

journal homepage: www.elsevier.com/locate/pacs

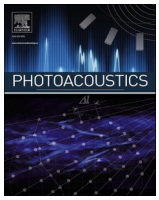

4D spectral-spatial computational photoacoustic dermoscopy

Yang Gao [a,b,c], Ting Feng [d,*], Haixia Qiu [e], Ying Gu [e], Qian Chen [a,c], Chao Zuo [a,b,c,*], Haigang Ma [a,b,c,*]

[a] Nanjing University of Science and Technology, School of Electronic and Optical Engineering, Smart Computational Imaging Laboratory (SCILab), Nanjing 210094, China
[b] Smart Computational Imaging Research Institute (SCIRI) of Nanjing University of Science and Technology, Nanjing 210094, China
[c] Nanjing University of Science and Technology, School of Electronic and Optical Engineering, Jiangsu Key Laboratory of Spectral Imaging & Intelligent Sense, Nanjing 210094, China
[d] Fudan University, Academy for Engineering and Technology, Shanghai 200433, China
[e] First Medical Center of PLA General Hospital, Beijing 100853, China

ARTICLE INFO

Keywords:
4D spectral-spatial
Skin imaging
Photoacoustic dermoscopy
Quantitative calculation
Learning from simulation

ABSTRACT

Photoacoustic dermoscopy (PAD) is an emerging non-invasive imaging technology aids in the diagnosis of dermatological conditions by obtaining optical absorption information of skin tissues. Despite advances in PAD, it remains unclear how to obtain quantitative accuracy of the reconstructed PAD images according to the optical and acoustic properties of multilayered skin, the wavelength and distribution of excitation light, and the detection performance of ultrasound transducers. In this work, a computing method of four-dimensional (4D) spectral-spatial imaging for PAD is developed to enable quantitative analysis and optimization of structural and functional imaging of skin. This method takes the optical and acoustic properties of heterogeneous skin tissues into account, which can be used to correct the optical field of excitation light, detectable ultrasonic field, and provide accurate single-spectrum analysis or multi-spectral imaging solutions of PAD for multilayered skin tissues. A series of experiments were performed, and simulation datasets obtained from the computational model were used to train neural networks to further improve the imaging quality of the PAD system. All the results demonstrated the method could contribute to the development and optimization of clinical PADs by datasets with multiple variable parameters, and provide clinical predictability of photoacoustic (PA) data for human skin.

1. Introduction

Skin is the largest organ of the human body, whose health is closely related to the whole body. Skin diseases, one of the most common ailments among humans, are characterized by structural and functional changes in the tissue components of the skin. Imaging technologies play an essential role in dermatology, providing non-invasive means of observation and diagnosis, and offering valuable information for clinical practitioners [1,2]. Traditional optical dermoscopy, such as confocal microscopy and optical coherence tomography, is limited to observing only the conformation of the epidermis and superficial dermis due to imaging depth constraints. Ultrasound imaging enables visualization of the entire skin structure through deep penetration, but its spatial resolution and ability to visualize microvasculature are poor, and it is unable to obtain metabolism-related biochemical information [3–5]. Photoacoustic imaging (PAI), an emerging imaging technology with both high spatial resolution and deep tissue imaging capabilities, has received widespread attention from the biomedical research community [6]. PAI is expected to bring more opportunities for the maintenance of skin health and the treatment of diseases.

As an effective application mode of PAI, photoacoustic dermoscopy (PAD), an emerging non-invasive imaging technique, can directly measure the optical absorption characteristics of tissues, thus facilitating the diagnosis of skin diseases [7]. PAD combines the advantages of optical and ultrasound imaging. By illuminating short-pulsed laser onto the skin, and then receiving the ultrasound signals generated by endogenous chromophores (hemoglobin, melanin, lipids, collagen, glucose, etc.), PAD can provide clinical practitioners with high-contrast and

* Corresponding authors at: Nanjing University of Science and Technology, School of Electronic and Optical Engineering, Smart Computational Imaging Laboratory (SCILab), Nanjing 210094, China.
E-mail addresses: gaoyang6613@njust.edu.cn (Y. Gao), fengting@fudan.edu.cn (T. Feng), qiuhxref@126.com (H. Qiu), guyinglaser301@163.com (Y. Gu), chenq@njust.edu.cn (Q. Chen), zuochao@njust.edu.cn (C. Zuo), mahaigang@njust.edu.cn (H. Ma).

https://doi.org/10.1016/j.pacs.2023.100572
Received 11 September 2023; Received in revised form 16 October 2023; Accepted 9 November 2023
Available online 10 November 2023

Table 1
The parameters of skin layers used in the computational model [23,35,43].

Layer	Thickness (mm)	W_k (%)	B_k (%)	M_k (%)	$\mu_s R_k$ (cm^{-1})	Velocity (m/s)	Density (kg/m^3)
Stratum corneum	0.01	0	0	1	80	1540	1500
Living epidermis	0.08	60	0	10	80	1720	1190
Papillary dermis	0.1	75	3	1	80	1650	1200
Upper blood plexus	0.08	75	3.8	0	40	1650	1200
Reticular dermis	1.2	75	3	0	40	1790	1200
Deep blood plexus	0.07	75	2.3	0	40	1540	1116
Subcutaneous fat	3	5	2.1	0	42	1450	971

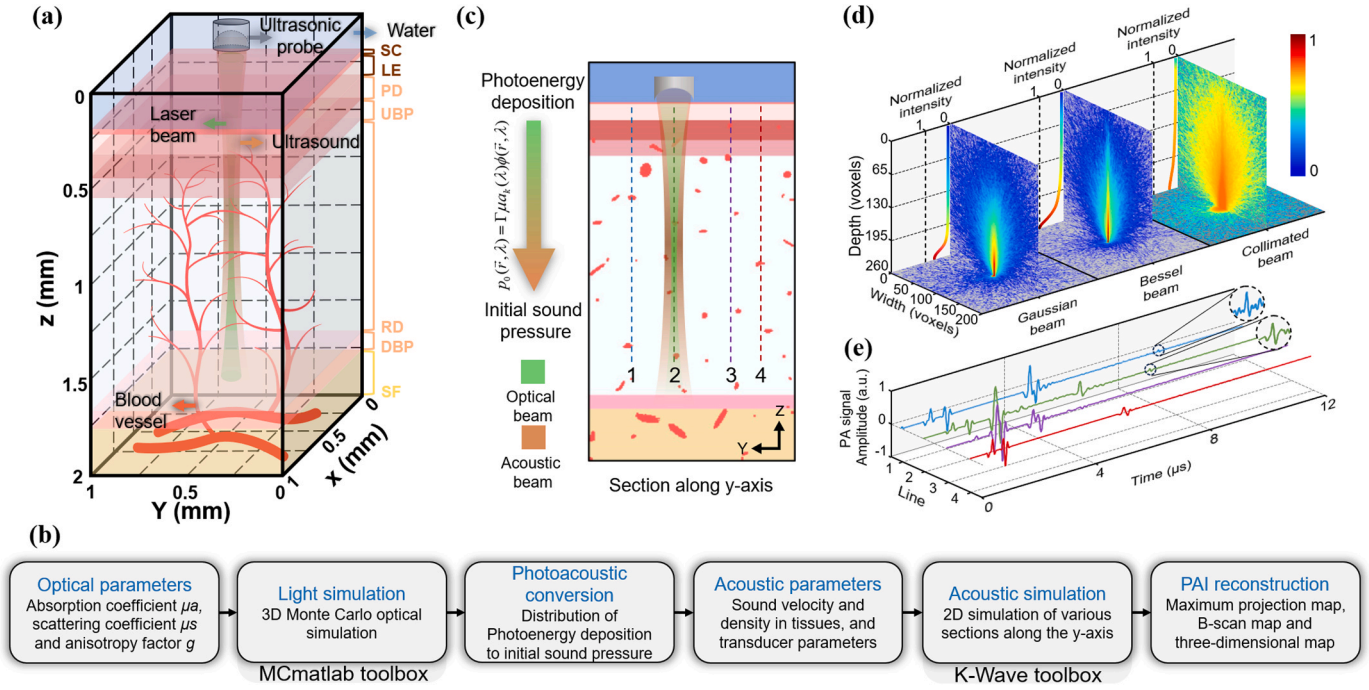

Fig. 1. 4D spectral-spatial computational model of skin. (a) Schematic diagram of a seven-layer skin model. SC: stratum corneum, LE: living epidermis, PD: papillary dermis, UBP: upper blood plexus, RD: reticular dermis, DBP: deep blood plexus, SF: subcutaneous fat. (b) Flowchart of key steps. (c) 2D simulation diagram. (d) Focused Gaussian beam, Bessel beam, collimated Gaussian beam photon distribution. (e) Photoacoustic signals along the dotted lines position in (c).

high-resolution morphological, functional, and pathological information of the skin, which has great potential in biomedical research and clinical applications [8]. In recent years, several PAD systems have been developed for imaging melanoma [9,10], café-au-lait macules [11], psoriasis [12], and skin blood vessels [13–15]. Despite the progress made in PAD research, there is still a lack of research on realistic modeling of the optical and acoustic properties of multilayered skin tissues for the quantitative accuracy of reconstructed PAD images caused by the wavelength and distribution of the excitation light, and the acoustic properties of the ultrasound transducer. The reliable computational methods can benefit the optimization design of the optical and acoustic parameters of PAD equipment.

Although deep learning has been used for PAI, most deep learning-based photoacoustic imaging needs thousands pairs of labeled input-output data to train the neural network, especially those applications in clinical skin imaging, which requires even larger amounts of data. It also should be noted that in many cases the ground truth corresponding to the experimental data is inaccessible. In such cases, an efficient "learning from computational model" scheme is urgently needed to obtain matching datasets. In addition, human skin tissues are multi-layered physiopathological structures with variability in optical absorption and acoustic impedance, which requires a rigorous computational model of the physical process of PAI.

The computational model of PAI, which encompasses both optical and acoustic simulations, plays a vital role. Various methodologies such as the radiative transfer equation [16], the finite element method [17], and the Monte Carlo (MC) method have been employed to simulate the scattering and absorption of light in tissues and to capture the distribution of luminous flux in tissues. Of these, the Monte Carlo method stands out as the gold standard, which is widely used to calculate the propagation of light in complex tissue structures [18–20]. However, many existing MC algorithms are for simpler layered tissue models [21–24]. Most models resort to representing skin as a single or triple-layered homogeneous medium, a simplification that often overlooks the intricate optical characteristics of multi-layered skin structures [25]. For the simulation of acoustics, tools such as the k-Wave toolbox [26] and the finite element method, with platforms like COMSOL, are predominant. The k-Wave, in particular, has gained traction due to its efficiency and simplicity [27–32]. Despite these advances, the current literature has limitations in certain aspects of photoacoustic dermoscopy (PAD) simulations, especially models that incorporate the intricate interactions between excitation optical fields and detectable ultrasonic fields. Furthermore, while multi-spectral PAI computational models have been explored [33,34], there is still molecular information on the depth- and wavelength-dependent multispectral PAD imaging that has not been studied enough for us to make authoritative statements.

In this study, we propose a photoacoustic hybrid 4D spectral-spatial computational model aimed at in-depth analysis of PAD skin structure

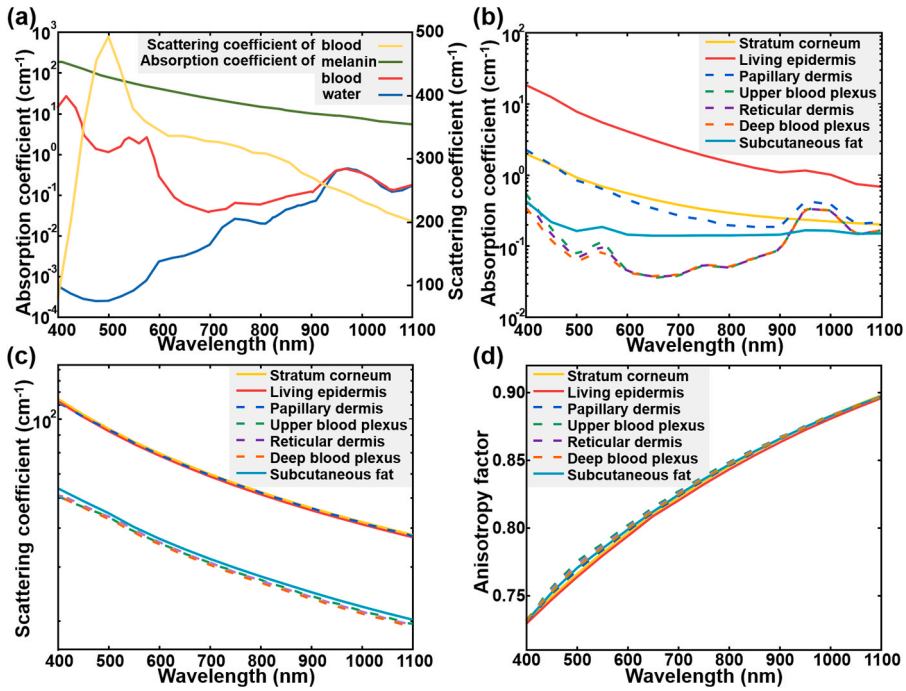

Fig. 2. The optical properties of each layer of the skin. (a) The absorption spectra of blood, melanin, and water, as well as the scattering spectra of blood [36,44–47]. (b) The absorption spectra of each layer of the seven-layer skin model. (c) Scattering spectrum. (d) Anisotropic factors.

and functional imaging for system optimization. Our model prioritizes the simulation of experimental scenarios as much as possible, adopts a point-by-point scanning mode based on photoacoustic microscopy, the model integrates forward propagation of light based on the Monte Carlo method and backward propagation of ultrasound computed based on k-Wave, and takes into account the multilayered heterogeneous structure of the skin as well as a specific vascular model, which makes the photoacoustic physical process of our proposed model on the more accurate. Furthermore, we have also incorporated the spectral dimension, achieving multispectral PAD imaging and unmixing with multiple beam types at varying wavelengths and energy levels. This allows for quantitative measurement of component intensities, which has the potential to greatly aid in disease diagnostic applications [10,34]. In addition, the model helps to accurately calibrate subcutaneous optical and acoustic distributions, providing a precise and optimized solution for imaging multilayered skin tissues using a PAD system. Finally, this study illustrates how the dataset obtained from our computational model can be utilized for neural network training to further break through hardware and biological constraints to improve the imaging quality of PAD experimental images.

The remainder of the paper is organized as follows: Section II describes the structure of the 4D spectral-spatial computational model, including the optical and acoustic properties of the tissue, the workflow of the computational model, the structure of the network model, the PAD experimental system and its quantitative optimization method. Section III presents a series of experimental results related to the reliability of the computational model. Also, the conclusion is summarized in Section IV.

2. Methodology

2.1. Simulation geometry

Here, the model defines a three-dimensional voxel grid with a size of 1 mm × 1 mm × 2 mm and a voxel count of 200 × 200 × 400 in each direction. A seven-layer skin model based on the anatomical structure of human skin (The skin model consists of seven layers: stratum corneum, living epidermis, papillary dermis, upper blood plexus, reticular dermis, deep blood plexus, and subcutaneous fat, respectively. The thickness of each layer is shown in Table 1.) is constructed, which is modeled as a multilayered planar medium [35]. The thermal and optical parameters of the multilayered skin tissues do not vary with temperature is assumed. Based on the physical, optical, and physiological properties of the cells, and the pigmentation content, the skin is subdivided into sublayers on the basis of a three-layer skin model [36]. The epidermis can be subdivided into two sublayers: the stratum corneum and the living epidermis. The stratum corneum is thin and flat, composed of dead squamous cells, with a high degree of keratinization, high fat and protein content, and relatively low water content. The living epidermis contains most of the skin pigments, mainly melanin [37]. The dermis is a vascularized layer, with the main absorbers in the visible spectrum being hemoglobin, carotenoids, and bilirubin. It can be subdivided into four layers: the papillary dermis, the upper vascular plexus, the reticular dermis, and the deep vascular plexus [38]. These subdivided layers and the subcutaneous adipose tissue layer constitute the seven-layer model, which is illustrated in Fig. 1a. The epidermis layer contains no blood tissue, and a three-dimensional vascular model publicly available from *Tetteh et al.* [39] is inserted beneath the epidermis layer of the model, as an approximation of the skin vasculature. Fig. 1b shows the flowchart of the key steps of the model, which is based on photoacoustic microscopy to realize PAD imaging, and Fig. 1c shows a two-dimensional (2D) schematic of the scanning process. Fig. 1d illustrates the three types of beams used in the study and their photon distributions, including focused Gaussian beam, Bessel beam, and collimated Gaussian beam. Imaging under the focused beam corresponds to confocal optical-resolution photoacoustic microscopy while imaging under the collimated Gaussian beam corresponds to acoustic-resolution photoacoustic microscopy. Fig. 1e shows the simulated photoacoustic signals along the position of the dashed line in Fig. 1c.

2.2. Optical properties of tissue

Skin is a complex multilayered heterogeneous tissue, and the depth and direction of light propagation within the skin are determined by the

optical properties of the various layers of tissue and blood vessels in the skin, which are wavelength dependent and vary according to the random inhomogeneous distribution of various chromophores and pigments [38]. For simplicity, each layer is typically treated as a homogeneous structure in the computational model, and the optical properties vary between layers but remain constant within each layer [28–33]. Typically, the optical properties of each skin layer include the absorption coefficient (μ_a), scattering coefficient (μ_s), anisotropy factor (g), and refractive index (n). The refractive index does not vary significantly between layers, and therefore, the refractive index can be set to a fixed value of 1.4 for all wavelengths and under all skin layers [40–42].

The absorption coefficient of each skin layer is mainly contributed by three basic chromophores: blood, melanin, and water. The variation of absorption coefficients with wavelength for these three components is illustrated in Fig. 2a. Table 1 lists the thickness of each layer and the relative amount of the three chromophores. The absorption coefficient of each layer μ_{a_k} can be calculated by Eq. 1 [23]:

$$\mu_{a\_k}(\lambda) = B_k\mu_{a\_blood}(\lambda) + M_k\mu_{a\_melanin}(\lambda) + W_k\mu_{a\_water}(\lambda) + (1 - B_k - M_k - W_k)\mu_{a\_background} \tag{1}$$

Where, k represents the number of layers, λ is the wavelength at which the absorption coefficient is being calculated, B_k, W_k, M_k are the volume fractions of blood, water, and melanin in the layer, respectively. μ_{a_blood}, μ_{a_water}, $\mu_{a\_melanin}$ and $\mu_{a\_background}$ represent the absorption coefficients of blood, water, melanin, and background tissue, respectively. It can be considered that $\mu_{a\_background}$ is independent of wavelength and is set as a fixed value of 0.15 cm^{-1} in the model. The calculated absorption spectra of each layer are presented in Fig. 2b.

The scattering coefficient of each skin layer in the model is mainly determined by blood. The variation of the scattering coefficient of blood with wavelength is illustrated in Fig. 2a. The scattering coefficient of each layer μ_{s_k} can be calculated using Eq. 2:

$$\mu_{s\_k}(\lambda) = B_kC_k\mu_{s\_blood}(\lambda) + (1 - B_k)\mu_sT_k(\lambda) \tag{2}$$

Where, the correction coefficient C_k is related to the diameter of blood vessels, it is assumed that the blood vessels in each skin layer have the same diameter, assuming $C_k = 0.2$. μ_{s_blood} represents the scattering coefficient of blood. The scattering coefficient $\mu_sT_k(\lambda)$ of bloodless tissue varies with wavelength. In this study, Eq. 3 was used to calculate:

$$\mu_sT_k(\lambda) = \mu_sR_k\left(\frac{577nm}{\lambda}\right) \tag{3}$$

Where, μ_sR_k is the scattering coefficient at the reference wavelength of 577 nm as shown in Table 1. The calculated scattering spectra of each layer are presented in Fig. 2c. The anisotropy factor $g_k(\lambda)$ can be expressed as Eq. 4:

$$g_k(\lambda) = \frac{B_kC_k\mu_{s\_blood}(\lambda)g_{blood} + (1 - B_k)\mu_sT_k(\lambda)gT(\lambda)}{\mu_{s\_k}(\lambda)} \tag{4}$$

Where, $gT(\lambda)$ is the anisotropy factor of bloodless tissue, obtained through Eq. 5:

$$gT(\lambda) = 0.7645 + 0.2355\left[1 - \exp\left(-\frac{\lambda - 500nm}{729.1nm}\right)\right] \tag{5}$$

The calculated anisotropy factors of each layer are presented in Fig. 2d.

2.3. Computational flowchart

This section describes the workflow of the 4D spectral-spatial computational PAD (Fig. 1b). The first step of the computation is to calculate the forward propagation of light in the tissue and the distribution of light energy deposition. We use the open-source Monte Carlo toolkit MCmatlab to solve this problem. The input beam is simulated by emitting photon packets and calculating their paths in the simulated body [47]. There are three beams available in the model: focused Gaussian beam, Bessel beam, and collimated Gaussian beam (Fig. 1d). The beam is incident vertically along the Z-axis of the model, when photon packets propagate from one voxel to another, some energy is deposited into the voxel based on its absorption coefficient. The deposited energy is numerically accumulated in a three-dimensional matrix, which is the light energy deposition distribution. The light energy deposition distribution is then converted into an initial pressure distribution matrix using Eq. 6:

$$p_0(r,\lambda) = \Gamma(r)\mu_{a\_k}(\lambda)\phi(r,\lambda) \tag{6}$$

Where, Γ is the Gruneisen parameter, which measures the conversion efficiency from light absorption to sound pressure. In the research conducted in this article, it is assumed that the homogeneity value of Γ is 0.2 [48]. $\mu_{a\_k}(\lambda)$ is the absorption coefficient of the corresponding dielectric layer k at position r at wavelength λ. $\phi(r, \lambda)$ is the luminous flux at position r at wavelength λ. Using the equation, the initial pressure values for each grid position in the model are obtained, and the propagation of photoacoustic waves to the transducer at each grid position is implemented using k-Wave [26].

The speed and density of ultrasound for each skin layer related to the acoustic computation are recorded in Table 1. The attenuation of acoustic waves plays a pivotal role in determining the acoustic properties of tissues. One of the primary contributors to this attenuation is acoustic absorption. This frequency (f) dependent attenuation is characterized using a power-law model. In the computational model of this paper, the acoustic attenuation coefficient of the tissue is taken as $1\ f^{1.5}$dB/cm/$MHz^{1.5}$. This signifies that the acoustic attenuation escalates in proportion to the frequency raised to the power of 1.5 [49,50]. A bowl-shaped focused ultrasound transducer is used in k-Wave with its focusing direction on the same axis as the center of the incident beam, and the center frequency and bandwidth are set accordingly to the experimental needs. Firstly, a 3D Monte Carlo optical computation is performed on the grid points on the scanning plane to obtain the light energy deposition distribution, which is then transformed to obtain the three-dimensional initial pressure distribution. Then, a 2D acoustic computation is performed on the plane of the scanning points along the Y-axis, and this process is repeated to achieve full scanning (Fig. 1c, e). A total of 160×160 A-line signals are obtained, resulting in a maximum-intensity projection image. Generating the light energy deposition distribution in the optical model takes approximately 6 s, and collecting the raw photoacoustic signals in the two-dimensional acoustic model takes approximately 2 s. All calculations are performed on an Intel Core i7–10700KF CPU and NVIDIA RTX A2000 GPU. Compared with the three-dimensional acoustic model, the scanning method using the two-dimensional acoustic model is approximately 30 times faster.

2.4. Network architecture

U-Net is an encoder-decoder structure network with skip connections, which helps to preserve the detailed information of the image and helps to mitigate the loss of information when recovering the resolution in the decoder stage. U-Net has a relatively small number of parameters and computational complexity, which makes it faster in training and inference and performs well in small sample cases [51]. In order to achieve further optimization of systematic imaging based on computationally generated datasets, a modified U-Net architecture is used in this study (shown in Fig. S1), where the network accepts a 624×624 grayscale image of skin blood vessels as input, the first layer contains 32 convolutional filters of size 3×3, and two successive convolution operations are activated by applying a leaky integer linear unit LReLU layer (slope 0.2), and then convolutional operation is implemented using a 2×2 convolutional layers instead of pooling to achieve downsampling, which allows the model to learn how best to reduce the spatial

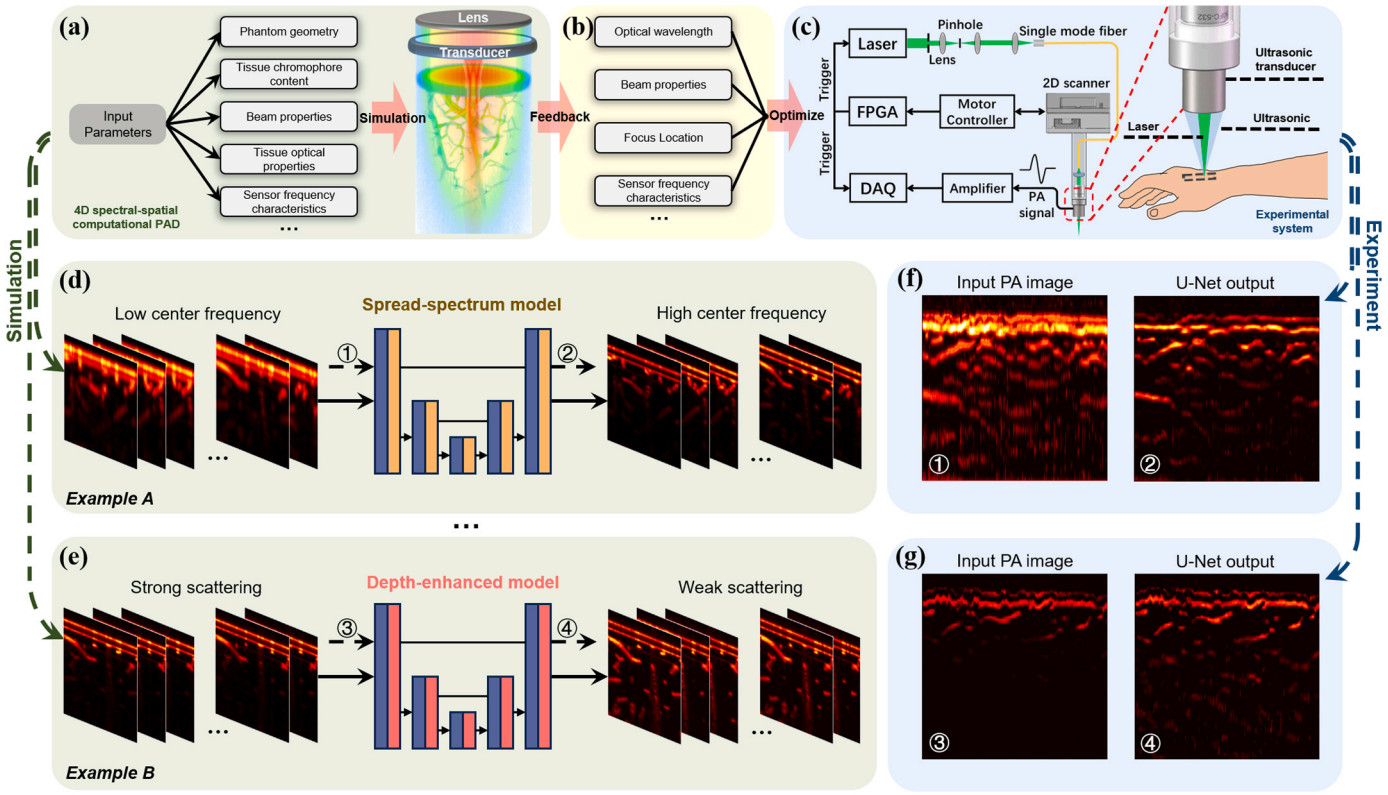

Fig. 3. The process of using the 4D spectral-spatial computational PAD combined with experiments for dataset acquisition and system optimization for deep learning. (a) Relevant parameters can be set before data acquisition, and the distribution of the model optical field and detector acoustic field under a collimated Gaussian beam in the model is shown. (b) Feedback on relevant performance optimization parameters is provided to the experimental system after simulating calculation. (c) Experimental system. (d) The dataset is used for training the spread-spectrum network model. (e) The dataset is used for training the depth-enhanced network model. (f) The low center frequency detector skin imaging results obtained in the experiment are input into the trained spread-spectrum model to obtain the output image. (g) The skin imaging results under conventional scattering obtained in the experiment are input into the trained depth-enhanced model to obtain the output image.

dimensions rather than relying on fixed operations, while better preserving certain features of the original input. The number of filters is incremented by powers of 2 up to the bottleneck layer, up to a maximum of 512 filters. The output is then upsampled using a 2×2 transpose convolution to obtain an output of the same size as the input, and then two successive convolution operations are applied again. The number of channels in each layer is gradually reduced symmetrically. Skip connections are added while the corresponding downsampled layer is upsampled. Finally, the output image is obtained by 1×1 convolutional downsampling. The total number of trainable parameters for the network is 8115009. The network is trained using the Adam optimizer's mean-square error (MSE) loss function ($\beta 1 = 0.8$, $\beta 2 = 0.999$), with the learning rate, the number of epochs, and the batch size set to 3e-4, 100, and 2, respectively. During the model training process, we evaluate the model using the validation dataset periodically to avoid overfitting. We evaluated the network performance using mean-square error (MSE), mean-absolute error (MAE), peak signal-to-noise ratio (PSNR), and structural similarity index (SSIM) on the simulated test dataset.

2.5. Experimental PAD imaging system

Fig. 3c shows the PAD imaging system employed for the experiment, using a 532 nm Q-switched pulsed laser (Talon 532–40, Spectra-Physics; pulse repetition rate of 10 kHz; pulse width of 20 ns) as a light source to excite the PA signal. The beam was passed through an optical spatial filter system and then coupled into a single-mode fiber with the help of a fiber coupler (PAF-X-7-A, Thorlabs Inc.). The fiber output laser beam was collimated by a fiber collimator (F240FC-532, Thorlab Inc.). Scanning was achieved by a two-dimensional linear motor (LS2–0830, JianCheng Technologies Ltd.) driven by a collimated light focused through a $5 \times$ objective lens (S Pian Apo HL 5x/0.13, SIGMA KOKI), and the signal was received by using a homemade hollow-bowl ultrasonic transducer, with a center frequency of 20 MHz and a bandwidth of about 100%. The laser fluence at the tissue surface was about 18 mJ/cm^2, which is below the ANSI safety limit of 20 mJ/cm^2. During raster scanning, the step between the two A-lines was 1 μm. The acquired PA signals were amplified by a 50 dB low-noise amplifier (LNA-650, RF Bay), and then the amplified PA signals were digitized using a high-speed data acquisition card (M4i.4480, Spectrum). The acquired data were recorded and reconstructed in real-time by a LabVIEW program.

2.6. Quantitatively optimal photoacoustic dermoscopy

The corresponding parameters in the 4D spectral-spatial computational model can be set according to the wavelength, energy density and focusing position of the incident beam used in the experimental PAD system as well as the frequency characteristics of the ultrasound transducer (Fig. 3a). The settings in this paper match the experimental system presented in Section 2.5. Adjusting its parameters based on the imaging results calculated by the model, iterating, and eventually feeding back relevant information to update the system's configuration to provide the best system parameters for the current application scenario (Fig. 3b), thus helping aiding in the optimization of the experimental PAD system (Fig. 3c). Meanwhile, the "learning from computational model" schemes are used to break through the limitations of hardware and human body in the experiments to further improve the imaging performance of the PAD system, such as the optimization of imaging resolution and depth. To train the spread-spectrum model (Fig. 3d), we set the center frequencies of the detectors in the k-Wave acoustic simulation to match the 20 MHz of the experimental system and the optimized target 60 MHz,

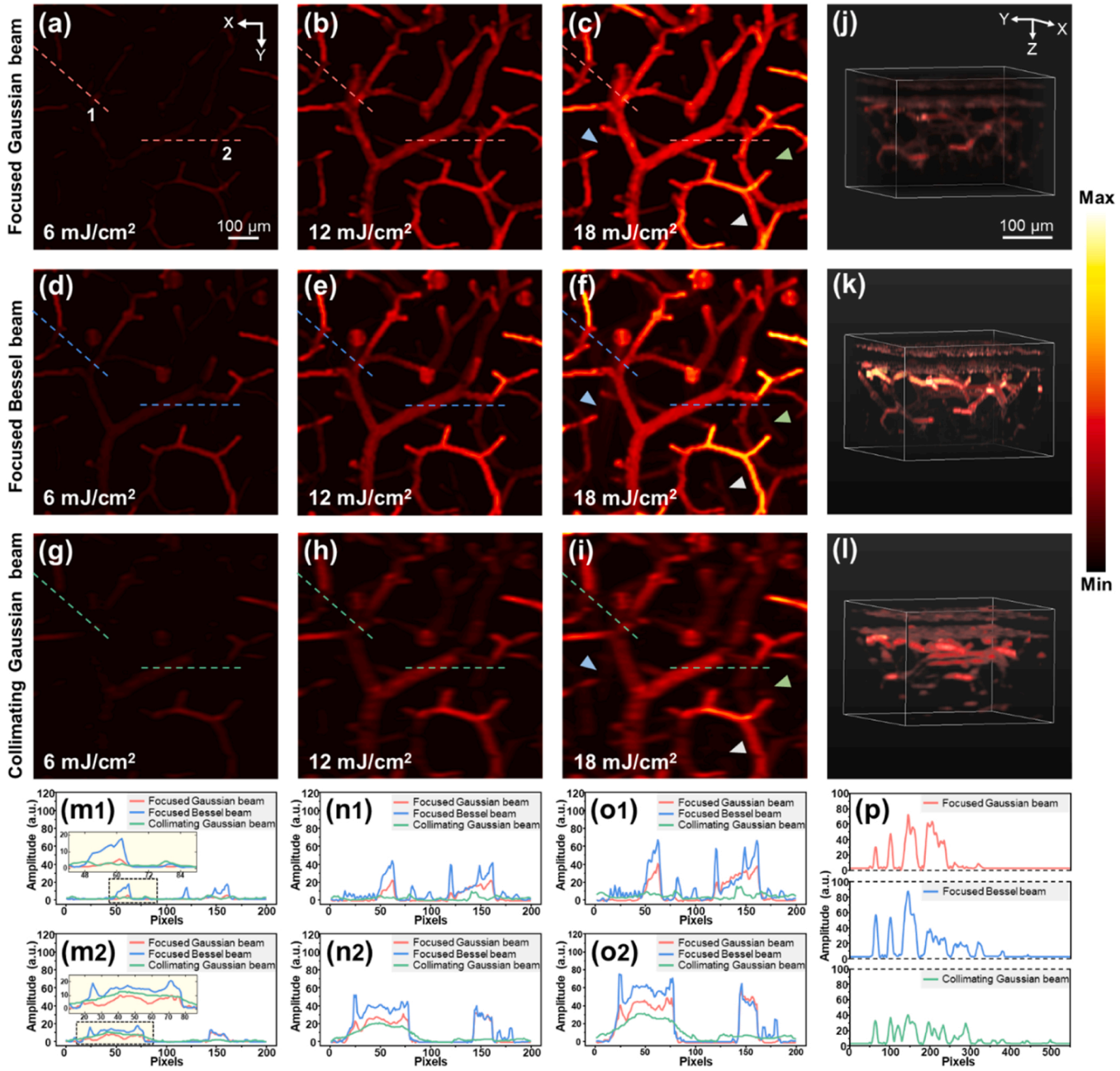

Fig. 4. Computational imaging results of (a-c) Focused Gaussian beam, (d-f) Bessel beam, and (g-i) collimated Gaussian beam when the power densities are 6 mJ/cm^2, 12 mJ/cm^2, and 18 mJ/cm^2. (j-l) The 3D imaging results of focused Gaussian beams, Bessel beams, and collimated Gaussian beams with a power density of 18 mJ/cm^2. (m1, m2) Profile intensity along dashed lines 1 and 2 in (a, d, g) with a power density of 6 mJ/cm^2. (n1, n2) Profile intensity along dashed lines 1 and 2 in (b, e, h) with a power density of 12 mJ/cm^2. (o1, o2) Profile intensity along dashed lines 1 and 2 in (c, f, i) with a power density of 18 mJ/cm^2. (p) The a-line signal envelope of three different beams at the same position with a power density of 18 mJ/cm^2.

respectively, and the data enhancement was achieved by horizontally flipping the 900 pairs of images generated by the computation. To ensure the robustness and generalization of the model, we divided the entire dataset into three parts: training, validation, and testing, where 1400 pairs of images were used for training, 200 pairs of images for validation, and 200 pairs of images for testing. For the deep-enhanced model (Fig. 3e), we set the optical scattering coefficient of the dermis as 1% as the ground truth parameter, and computationally obtained 900 pairs of images corresponding to the dermis under strong and weak scattering, which helps to obtain deeper PAD imaging information, and likewise realized the data enhancement by horizontal flipping, whose number of the training, validation, and testing sets are also 1400, 200, 200, respectively. More broadly, the corresponding parameters in the computational model are set according to the PAD experimental system and the desired experimental results, and the matched datasets are obtained for network training and adjusted within a certain range to increase the diversity of the data in order to obtain a good generalization performance. Finally, by combining the trained network with the PAD experimental system, the optimized imaging results after network processing can be quickly obtained.

3. Results and discussions

This section describes experiments on four factors that affect the imaging performance of the 4D spectral-spatial computational model, as well as the acquisition of the dataset and its application in deep learning.

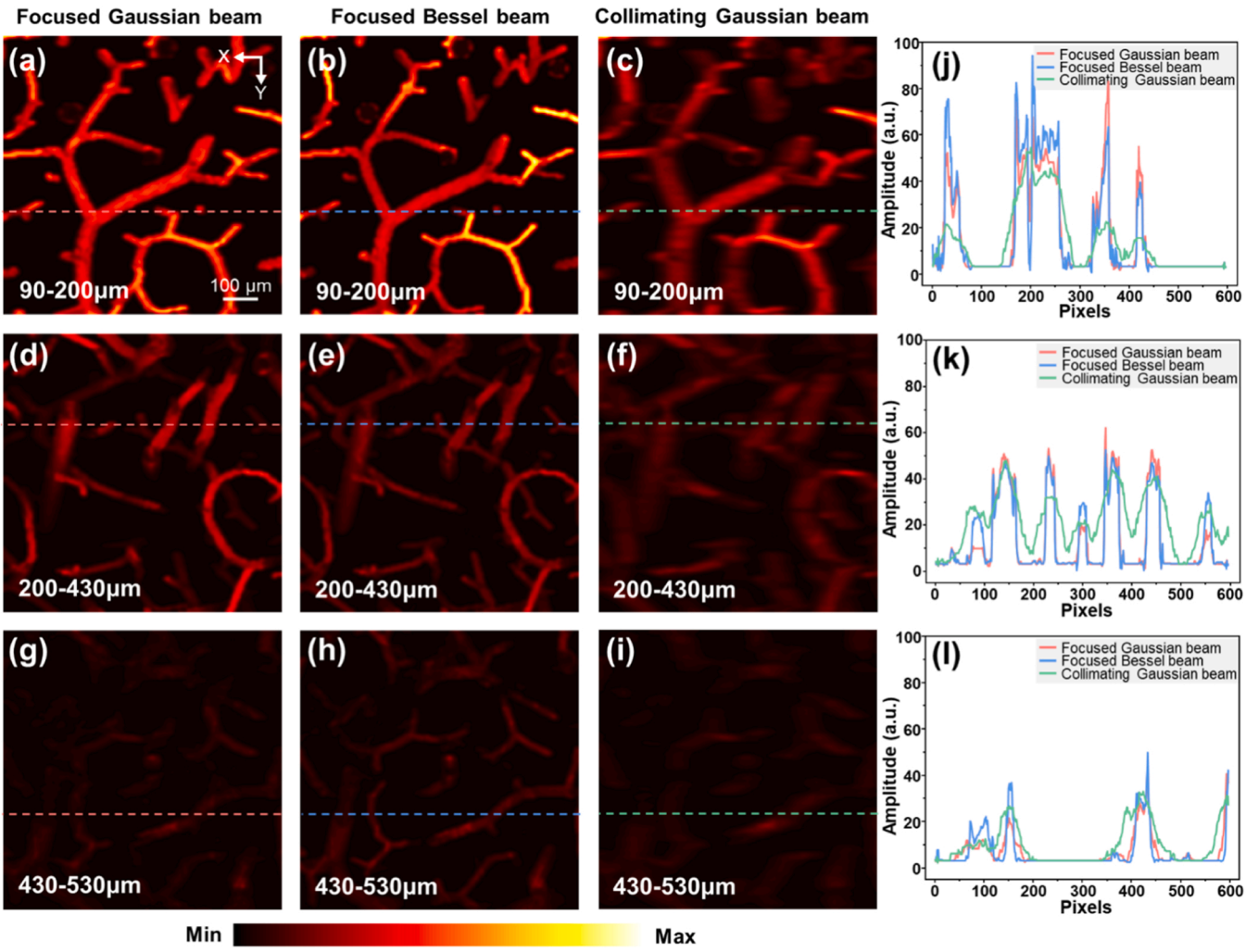

Fig. 5. Maximum intensity projection results of focused Gaussian beam, Bessel beam, and collimated Gaussian beam at different depths with a power density of 18 mJ/cm^2. (a-c) Maximum projection image from 90 to 200 μm. (d-f) Maximum projection image from 200 to 430 μm. (g-i) Maximum projection image from 430 to 530 μm. (j) Profile intensity along the dashed lines in (a-c). (k) Profile intensity along the dashed lines in (d-f). (l) Profile intensity along the dashed lines in (g-i).

Section 3.1 discusses the influence of the type of incident beam and the power density on the PAD imaging performance. Section 3.2 describes the influence of ultrasound transducers with different center frequencies and bandwidths on the PAD imaging performance. Section 3.3 presents the imaging results of Gaussian beams focused at different depths beneath the skin. Section 3.4 describes the imaging depth under different wavelength beams, demonstrating the multispectral imaging capability of the model. Section 3.5 discusses the feasibility of generating datasets for neural network training using the model.

3.1. *The influence of the incident beam*

The laser parameters used in PAI can greatly affect the imaging results, and since the calculation of the light energy deposition distribution and ultrasonic back propagation of the computational model is performed in a stepwise manner, it can be assumed that the imaging is not affected by the laser pulse width. To validate the influence of beam focusing and energy on imaging performance in the computational model, focused Gaussian, Bessel, and collimated Gaussian beams with varying power densities of incident beams at a wavelength of 532 nm were used for imaging while the optical and acoustic parameters of the model were fixed. The Gaussian and Bessel beams were focused on the boundary between the epidermis and dermis layers of the skin model, and full scanning was performed on the same vascular network for each type of beam. The ultrasonic transducer with a center frequency of 100 MHz and a bandwidth of 100% was used to receive photoacoustic signals to reduce measurement errors in the computational model. Fig. 4a-c, d-f, and g-i show the maximum intensity projection results of the three types of beams with power densities of 6 mJ/cm^2, 12 mJ/cm^2, and 18 mJ/cm^2, respectively. Fig. 4j-l show the three-dimensional imaging results of the three types of beams with a power density of 18 mJ/cm^2. Fig. 5 shows the maximum intensity projection results at different depths of the three types of beams with a power density of 18 mJ/cm^2, in which we could clearly see the difference in imaging depth and resolution between the three beams. The comparisons in Figs. 4m-p and 5 show that, with a fixed power density, Bessel beams and collimated Gaussian beams can achieve greater imaging depth, while Bessel beams have a higher lateral resolution.

In PAI, the intensity of the PA signal is directly proportional to the local optical fluence [52]. Increasing the power density of the incident beam directly increases the optical fluence, which enhances the signal intensity and amplifies small signals in deeper regions, thereby improving the visibility of targets in deeper regions. The imaging resolution is closely related to the size of the optical focus [53]. The collimated Gaussian beams have the lowest imaging quality due to the lack of focus. Both focused Gaussian beams and Bessel beams have excellent spot sizes at the focus point, but Bessel beams achieve better imaging results due to their larger depth of field [54,55]. This result is consistent

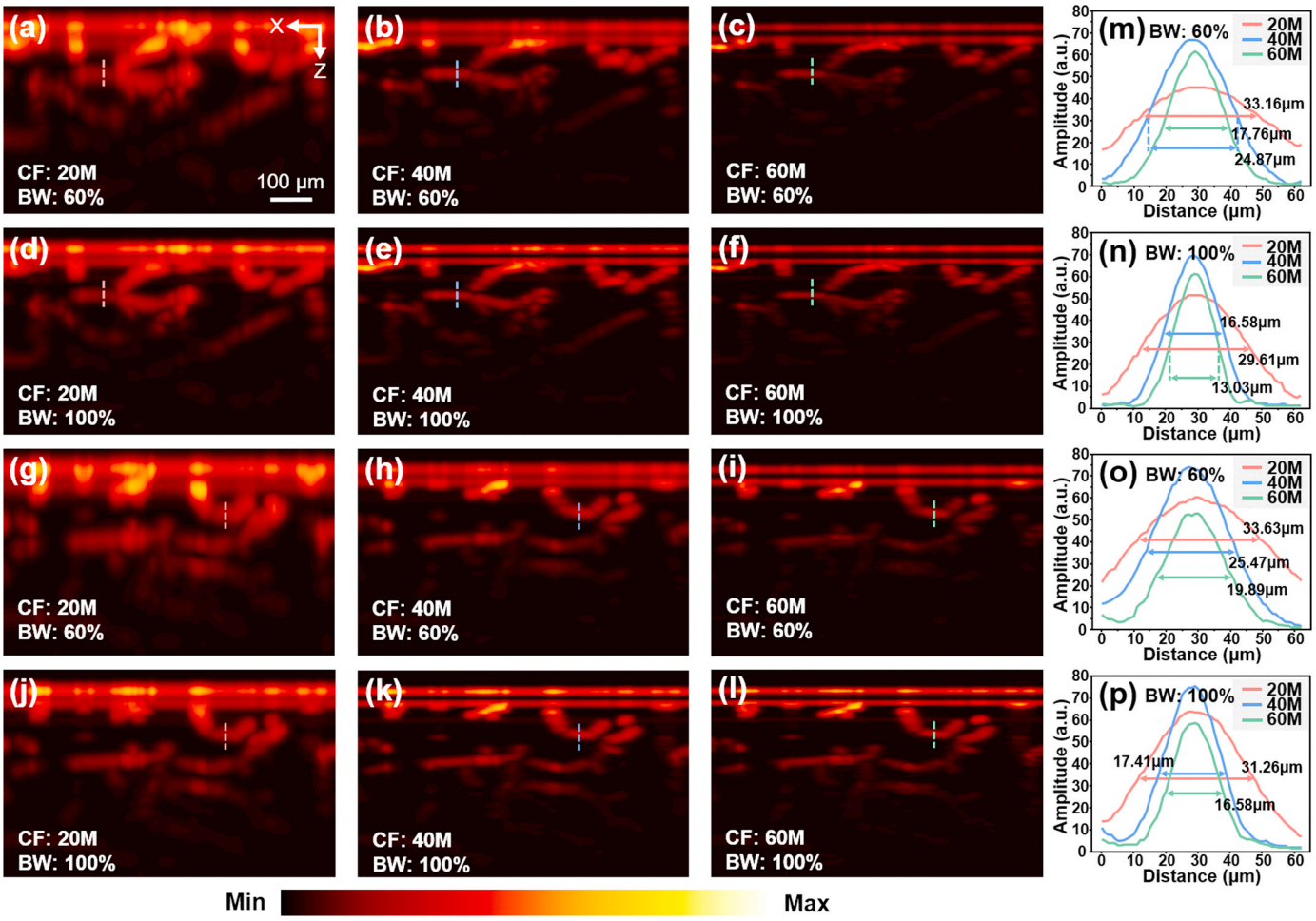

Fig. 6. Computational imaging results of ultrasonic transducers at different center frequencies and bandwidths. (a-c) Position 1 with center frequencies of 20 MHz, 40 MHz, and 60 MHz and a bandwidth of 60%. (d-f) Position 1 with center frequencies of 20 MHz, 40 MHz, and 60 MHz and a bandwidth of 100%. (g-i) Position 2 with center frequencies of 20 MHz, 40 MHz, 60 MHz, and 60% bandwidth. (j-l) Position 2 with center frequencies of 20 MHz, 40 MHz, 60 MHz, and 100% bandwidth. (m) PA amplitude along the dashed lines in images (a-c). (n) PA amplitude along the dashed lines in images (d-f). (o) PA amplitude along the dashed lines in images (g-i). (p) PA amplitude along the dashed lines in (j-l).

with reality and confirms the reliability of the proposed computational optical model in this work.

3.2. *The influence of ultrasonic transducer performance*

The human skin generates broadband PA signals ranging from a few to hundreds of MHz due to the wide variation in the size of light absorbers. The central frequency and bandwidth of the transducer for detection must be selected based on the size of the target [56]. However, the improper selection of detection bandwidth and central frequency in most PAD studies has resulted in many skin structures being indistinguishable [57].

In this section, under the condition of unchanged optical parameters of the model, in order to reduce the impact of beam focusing on imaging depth, we investigated the effects of changing the center frequency and bandwidth of the ultrasonic transducer on the PAD imaging performance when using a collimated Gaussian beam for illumination of 532 nm. The detection sensitivity of the ultrasonic transducer is higher near the acoustic focus, and its depth of field mainly depends on the center frequency and the numerical aperture of the acoustic lens, typically several hundred micrometers, which is comparable to the depth of field of a Bessel beam. The computational model used in this study employed a bowl-shaped focused ultrasonic transducer consisting of several point detectors on a grid, whose directionality comes from the spatial average of the pressure field on the detector surface. The depth of field extends along the entire central axis, and it can be assumed that the detection sensitivity of the transducer is uniform within the depth of field range.

In this study, the center frequency of the ultrasonic transducer was chosen as 20 MHz, 40 MHz, and 60 MHz, and the bandwidth was increased from 60% to 100%. The imaging results under different combinations of parameters are shown in Fig. 6a-l, and the profile intensities along the dashed line in the figures are shown in Fig. 6m-p, which show that the axial resolution improves with the increase of the center frequency and bandwidth of the transducer. In addition, due to the correlation between sound attenuation and frequency, as the central frequency of the transducer increases, the visibility of deep blood vessels becomes weaker. These imaging results highlight the benefits of using ultra-broadband ultrasound detectors in PAD.

3.3. *The influence of laser focusing position*

In imaging and diagnostics of PAD, lateral resolution is critical for tissue microstructure studies. Usually, there is a compromise between imaging depth and resolution. Imaging resolution can be improved by beam focusing, but defocusing occurs when the beam is focused at a certain depth under the skin, at which point the imaging resolution deteriorates rapidly. Conversely, if the focusing depth is too shallow, the

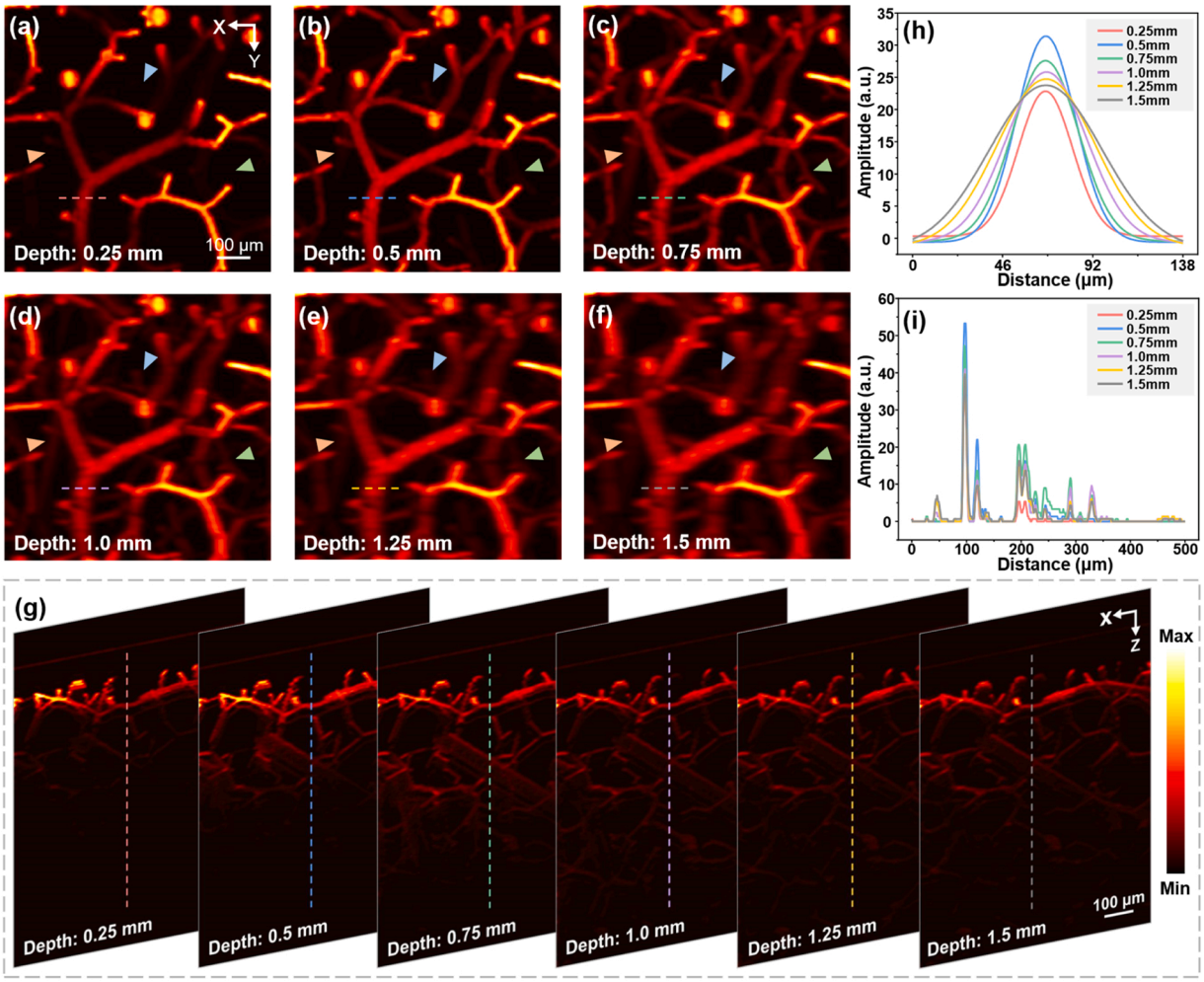

Fig. 7. The imaging results when the Gaussian beam is focused at 0.25 mm, 0.5 mm, 0.75 mm, 1.0 mm, 1.25 mm, and 1.5 mm. (a-f) X-Y maximum projection image. (g) X-Z maximum projection image. (h) PA amplitude along the dashed lines in (a-f). (i) PA amplitude along the dashed lines in (g).

imaging depth may not meet the clinical requirements.

This section discusses the effect of the focusing depth of the incident focused Gaussian beam at 532 nm on imaging. The optical parameters of the skin model remained unchanged, and the incident beam power density was 18 mJ/cm^2. The center frequency of the ultrasonic transducer was set to 100 MHz, with a bandwidth of 80%. Full-scan imaging was performed at six different depths where the Gaussian beam was focused at 0.25 mm, 0.5 mm, 0.75 mm, 1.0 mm, 1.25 mm, and 1.5 mm, respectively. Fig. 7a-f show the maximum projection imaging results in the X-Y plane at these six different focusing depths, Fig. 7g shows the maximum projection results in the X-Z plane, and Fig. 7h and i show the normalized profile intensity along the white dashed lines in Fig. 7a-g. As the focusing depth increases, the imaging depth is improved within the maximum range, but the upper vessels are gradually out of focus, leading to a deterioration in the lateral resolution of the imaging. The best imaging results were obtained when the depth of focus was 0.75 mm, which may be because the ultrasound transducer we used in the simulation may have the best focus at this particular depth and the focused Gaussian beam used still maintains a good spot at this depth due to the optical properties of the tissue. However, this observation is not necessarily universally applicable in all cases. Different experimental systems, different samples, and different experimental conditions may affect the determination of the optimal depth of focus.

3.4. Multi-spectral photoacoustic imaging and spectral unmixing

Different skin layers have different optical absorption and scattering properties for different wavelengths, resulting in different penetration depths for each wavelength beam. To further investigate the effect of such wavelengths on the penetration depth, an incident collimated Gaussian beam was used in this section, and computational measurements of imaging depth were made at 50 nm intervals for 15 wavelengths in the wavelength range from 400 nm to 1100 nm. As shown in Fig. 8a, we plotted the fluence rate of incident light at each wavelength up to 80%, 60%, 40%, 20%, 10%, and 5% as a function of penetration depth. As can be seen from the plots, as the wavelength increases, the corresponding penetration depth increases, which is consistent with our expected results. This result suggests that in skin imaging applications, the selection of appropriate wavelengths can realize deeper imaging.

Next, the multi-spectral imaging capability of the proposed model was verified by simulation experiments. Here, we updated the components of the vascular structure in the computational model to a combination of hemoglobin (Hb), oxyhemoglobin (HbO_2), Lipid, and Glucose. The epidermal components only contain lipids, and the variation of optical absorption coefficients of wavelength for the four components is shown in Fig. 8b. B-scan images were acquired at wavelengths ranging from 700 nm to 1100 nm at 25 nm intervals for a total of 17 wavelengths using a collimated Gaussian beam and an ultrasound transducer with a center frequency of 100 MHz and a bandwidth of 100%. Fig. 8c shows the imaging results at seven representative wavelengths: 700 nm,

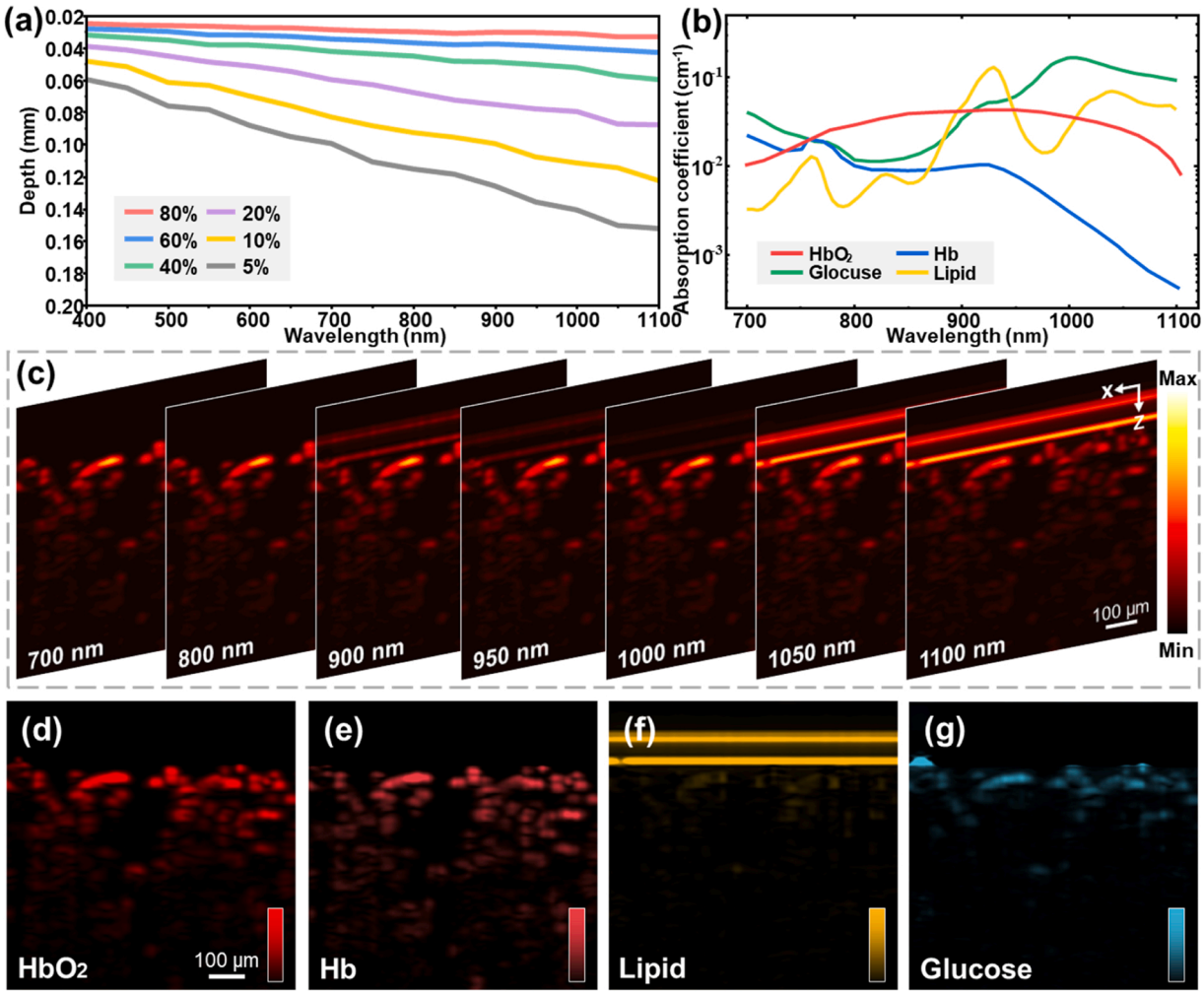

Fig. 8. Multi-spectral imaging and spectral unmixing results. (a)When the fluence rate of incident light reaches 80%, 60%, 40%, 20%, 10%, and 5%, the depth of penetration into the skin varies with the wavelength of the incident light. The fluence rate value is taken from the central column of the output fluence rate grid. (b) Plots of optical absorption coefficients as a function of wavelength for Hb, HbO_2, Lipid, and Glucose. (c) B-scan images at 700 nm, 800 nm, 900 nm, 950 nm, 1000 nm, 1050 nm, and 1100 nm wavelengths. (d-g) Corresponding spectral unmixing results.

Table 2
Quantitative comparison between ground truth and simulated/U-Net output images on test dataset in the spread-spectrum model.The metrics are represented in the form of mean ± standard deviation.

	MAE	MSE	PSNR	SSIM
Simulated images	0.0543 ± 0.0077	0.1562 ± 0.0040	66.3208 ± 1.0247 dB	0.8115 ± 0.1418
U-Net output images	0.0042 ± 0.0009	0.0001 ± 0.0001	87.4351 ± 1.9440 dB	0.9908 ± 0.0016

Table 3
Quantitative comparison between ground truth and simulated/U-Net output images on test dataset in the depth-enhanced model.The metrics are represented in the form of mean ± standard deviation.

	MAE	MSE	PSNR	SSIM
Simulated images	0.0138 ± 0.0054	0.0019 ± 0.0018	77.0055 ± 3.6093 dB	0.9308 ± 0.0228
U-Net output images	0.0066 ± 0.0029	0.0003 ± 0.0004	84.9128 ± 3.3614 dB	0.9647 ± 0.0239

800 nm, 900 nm, 950 nm, 1000 nm, 1050 nm, and 1100 nm. It can be seen that at the wavelengths of 700 nm and 800 nm, lipids are in the absorption valley, which does not show up clearly in the resulting images, and near 900 nm and 950 nm, HbO_2 is at the absorption peak, which absorbs light more strongly and is shown with higher contrast in the image. The multi-wavelength PA data were utilized to decompose the absorption spectra of the mixed targets by a non-negative constrained least-squares algorithm [58] to obtain unmixed images of the four components, Hb, HbO_2, Lipid, and Glucose, as shown in Fig. 8d-g. The unmixing results show a decreasing trend with increasing depth because the intensity of the photoacoustic signals produced by each component decreases gradually at the depth of the tissue due to the consideration of the fluence heterogeneity in the optical forward simulation, especially for lower concentrations of glucose. The unmixing results were in close agreement with the modeled components. The multispectral imaging and unmixing capabilities of the skin computational model are useful for the development and optimization of multiwavelength PAD systems, and the analysis of biochemical components in conjunction with spectral unmixing algorithms can help to more accurately diagnose skin diseases.

3.5. *Dataset acquisition and assistance in system optimization*

Deep learning is being widely researched for medical image analysis

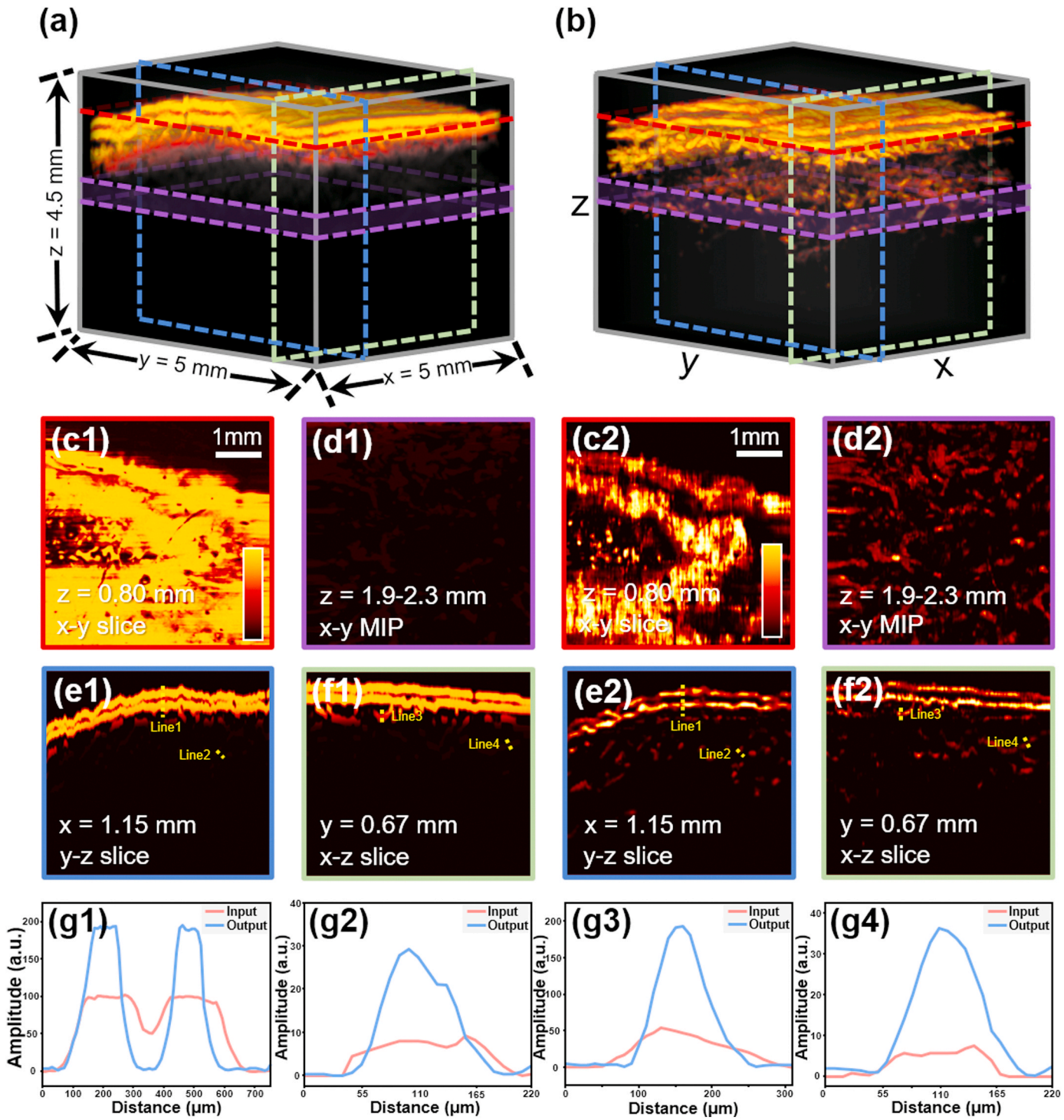

Fig. 9. Network generalization test results. (a) 3D PA image of palm skin. (b) 3D PA image obtained after the spread-spectrum network and the depth-enhanced network processing. (c1, c2) X-Y slice images of red dashed line position in the 3D images. (d1, d2) X-Y maximum intensity projection (MIP) of the purple dashed range in the 3D images. (e1, e2)Y-Z slice images of blue dashed line position in the 3D images. (f1, f2) X-Z slice images of green dashed line position in the 3D images. (g1-g4) Profile intensity along the yellow dashed lines in the slice images.

and processing [59–64]. Most of the deep learning techniques currently used in photoacoustic imaging belong to supervised learning. To train the network, it is essential to establish a matched dataset that pairs ground truth with corresponding measurements. Ideally, datasets should be collected through physical experiments based on the same imaging system. However, in many cases, it is difficult to obtain the ground truth corresponding to the experimental data. In such cases, matching datasets can be obtained through "learning from computational model" schemes [65–67]. The 4D spectral-spatial computational model in this paper considers wavelength-dependent optical scattering and can calculate the optical and acoustic characteristics of real heterogeneous skin tissue, generating multi-spectral photoacoustic skin imaging datasets under various physical conditions.

Data acquisition requires setting the relevant parameters according to the expected ground truth, including phantom geometry, tissue chromophore content, beam properties, tissue optical properties, sensor

frequency characteristics, etc. This process is shown in Fig. 3a. The optimal system parameters are obtained based on the feedback during the calculation (Fig. 3b), which can assist in optimizing the experimental system (Fig. 3c). Here are two examples illustrating how to implement the "learning from computational model" schemes.

For photoacoustic skin vascular imaging, ultrasound transducers with large center frequencies and wide bandwidths are able to capture fine structural information of blood vessels and obtain higher axial resolution. However, the price of ultrasound transducers is closely related to their performance, and in order to reduce the cost of system construction and data collection, the image spread spectrum can be realized by training the network with simulated data (Fig. 3d). Here, the training of the spread-spectrum network was implemented based on U-Net and the performance of the network on the test set is shown in Table 2. Then it was tested on the experimental PAI data. Again, the experimental system used an ultrasonic detector with a center frequency of 20 MHz, and the scanned PA images of the skin on the back of the author's hand were fed into the trained spectral spreading network, and the axial resolution of the output image and the completeness of the image information were significantly improved (Fig. 3f).

In addition, since photoacoustic imaging depth is largely affected by optical scattering and optical removal of human skin is difficult to achieve, it is of great significance to train the network to enhance the imaging depth by calculated data. The same network architecture was used to train the depth-enhanced network (Fig. 3e) to help obtain deeper information about PAD imaging. The evaluated parameter values on the test dataset are shown in Table 3. The test results on a priori known leaf sample are shown in Fig. S3. Further, the depth-enhanced network was tested with skin vascularization experimental datas, and the visibility of deeper information in the output image was greatly improved (Fig. 3g).

To examine the generalization of the trained neural network model, here the experimentally acquired 3D skin photoacoustic imaging data of 5 mm × 5 mm × 4.5 mm were sequentially fed into the spread spectrum network and depth-enhanced network trained in the above examples with the form of X-Z slices, which have different epidermal shapes and vascular structures. The slices obtained from the network output were reconstructed into 3D images, and Fig. 9 shows the imaging results before and after network processing. It can be clearly seen that the axial resolution of the image is improved and deeper blood vessels are shown. The above experimental results show that the simulated data obtained using the PAD computational model proposed in this paper can obtain results similar to those of actual skin imaging, and can be used to train the network well, thus significantly reducing the training cost.

4. Conclusion

In this paper, we proposed and validated a hybrid computational method of 4D of spectral-spatial imaging for quantitative PAD, which enables structural and molecular computational imaging of blood vessels. The method fully considers wavelength-dependent optical scattering and can calculate the optical and acoustic properties of heterogeneous skin tissue. The computational model integrates two open-source toolboxes: MCmatlab for forward propagation Monte Carlo model of light and calculation of light flux at each grid position, and k-Wave for computation of ultrasonic propagation and reception. By adjusting the types of incident beams, the optical focusing depth, the center frequency, and the bandwidth of the ultrasound transducer, imaging experiments were performed to demonstrate that the computational model can calculate the effects of actual optical and acoustic parameters on photoacoustic imaging and validate its 3D imaging capability. The molecular information obtained for depth- and wavelength-dependent multi-spectral PAD imaging through multi-spectral imaging of Hb, HbO_2, Lipid, Glucose, and least-squares unmixing of mixed components. In addition to the above experiments, the phantom structure, optical and acoustic parameters can be flexibly set according to the needs to realize the calculated imaging under various possible variations of multi-scenarios, including skin color, skin thickness, blood vessel number, size and shape, and tissue thickness. The feasibility of simulated datasets generated by computational modeling for neural network training was also demonstrated, helping to solve the major challenge of deep learning techniques in photoacoustic skin imaging that cannot obtain ground truth in many cases, with the potential to further improve the imaging quality of the PAD system through image reconstruction, information processing, and artificial intelligence methods.

In summary, this study provided a comprehensive investigation of the photoacoustic mechanisms in skin tissue, laying a theoretical foundation for the application of photoacoustic imaging detection technology in skin disease diagnosis and treatment, providing a reference for the improvement of treatment protocols, which is crucial for understanding the photoacoustic properties of dermatological diseases and subcutaneous tissues, interpreting and quantifying the diagnostic data as well as evaluating therapeutic and surgical protocols, and also providing a powerful tool for the performance of PAD devices in preclinical and clinical applications. In addition, the PAD computational model proposed in this work can simulate skin tissue, and imaging for specific applications and generate corresponding datasets on a large scale, contributing to the artificial intelligence applications in the PAD field.

Finally, it should be mentioned that, although the "learning from computational model" schemes remove the reliance on large amounts of labeled experimental data, the inconsistency between the image formation model and the actual experimental conditions leads to additional "domain adaptation" challenges. Although in this work we have demonstrated how the model can be utilized to obtain ground truth datasets that are difficult to access in experiments for neural network training, in practice, extending the computational model can be challenging due to a limited understanding of experimental perturbations, such as various noises, aberrations, vibrations, and motion artifacts, and the challenge of not being able to realistically and comprehensively reflect the real experimental system still exists. In future work, we will strive to address the approximate modeling related to these factors and extend the application scenarios of computational models.

Declaration of Competing Interest

The authors declare that they have no known competing financial interests or personal relationships that could have appeared to influence the work reported in this paper.

Data Availability

Code underlying the results presented in this paper may be obtained from the corresponding author upon reasonable request.

Acknowledgements

This work was supported by National Natural Science Foundation of China (62275121, 12204239, 61835015, 1237040502), Youth Foundation of Jiangsu Province (BK20220946), Fundamental Research Funds for the Central Universities (30923011024).

Appendix A. Supporting information

Supplementary data associated with this article can be found in the online version at doi:10.1016/j.pacs.2023.100572.

References

[1] E. Berardesca, H. Maibach, K. Wilhelm. Non-Invasive Diagnostic Techniques in Clinical Dermatology, Springer Science & Business Media, Berlin, 2013.
[2] P. Beard, Biomedical photoacoustic imaging, 602-31, Interface Focus 1 (4) (2011), https://doi.org/10.1098/rsfs.2011.0028.

[3] H. Kittler, H. Pehamberger, K. Wolff, Diagnostic accuracy of dermoscopy, Lancet Oncol. 3 (3) (2002) 159–165, https://doi.org/10.1016/S1470-2045(02)00679-4.

[4] J. Kim, E. Park, W. Choi, B. Park, K.J. Lee, C. Kim, Clinical photoacoustic/ultrasound imaging: systems and applications, TM3B.5, Clin. Trans. Biophot. 01 (2020), https://doi.org/10.1364/TRANSLATIONAL.2020.TM3B.5.

[5] A.J. Deegan, J. Lu, R. Sharma, S.P. Mandell, R.K. Wang, Imaging human skin autograft integration with optical coherence tomography, Quant. Imaging Med Surg. 11 (2) (2021) 784–796, https://doi.org/10.21037/qims-20-750.

[6] L.V. Wang, S. Hu, Photoacoustic tomography: in vivo imaging from organelles to organs, Science 335 (6075) (2012) 1458–1462, https://doi.org/10.1126/science.1216210.

[7] H.F. Zhang, K.I. Maslov, L.V. Wang, Automatic algorithm for skin profile detection in photoacoustic microscopy, J. Biomed. Opt. 14 (2) (2009), 024050, https://doi.org/10.1117/1.3122362.

[8] I. Steinberg, D.M. Hulandad, O. Vermesh, H.E. Frostig, W.S. Tummers, S. S. Gambhir, Photoacoustic clinical imaging, Photoacoustics 14 (2019) 77–98, https://doi.org/10.1016/j.pacs.2019.05.001.

[9] P. Hai, Y. Li, L. Zhu, L. Shmuylovich, L.A. Cornelius, L.V. Wang, Label-free high-throughput photoacoustic tomography of suspected circulating melanoma tumor cells in patients in vivo, J. Biomed. Opt. 25 (3) (2020), 036002, https://doi.org/10.1117/1.JBO.25.3.036002.

[10] J. Kim, Y.H. Kim, B. Park, H.M. Seo, C.H. Bang, G.S. Park, Y.M. Park, J.W. Rhie, J. H. Lee, C. Kim, Br.J. Dermatol, Multispectral ex vivo photoacoustic imaging of cutaneous melanoma for better selection of the excision margin, Br. J. Dermatol. 179 (3) (2018) 780–782, https://doi.org/10.1111/bjd.16677.

[11] H.G. Ma, Z.Y. Wang, Z.W. Cheng, G. He, T. Feng, C. Zuo, H.X. Qiu, Multiscale confocal photoacoustic dermoscopy to evaluate skin health, Quant. Imaging Med. Surg. 12 (5) (2023) 2696–2708, https://doi.org/10.21037/qims-21-878.

[12] J. Aguirre, M. Schwarz, N. Garzorz, M. Omar, A. Buehler, K. Eyerich, V. Ntziachristos, Precision assessment of label-free psoriasis biomarkers with ultra-broadband optoacoustic mesoscopy, Nat. Biomed. Eng. 1 (2017) 0068, https://doi.org/10.1038/s41551-017-0068.

[13] H.G. Ma, Z.W. Cheng, Z.Y. Wang, W.Y. Zhang, S.H. Yang, Switchable optical and acoustic resolution photoacoustic dermoscope dedicated into in vivo biopsy-like of human skin, Appl. Phys. Lett. 1l16 (7) (2020), 073703, https://doi.org/10.1063/1.5143155.

[14] H.G. Ma, Z.W. Cheng, Z.Y. Wang, H.X. Qiu, T.D. Shen, D. Xing, Y. Gu, S.H. Yang, Quantitative and anatomical imaging of dermal angiopathy by noninvasive photoacoustic microscopic biopsy, Biomed. Opt. Express 12 (2021) 6300–6316, https://doi.org/10.1364/BOE.439625.

[15] J. Ahn, J.Y. Kim, W. Choi, C. Kim, High-resolution functional photoacoustic monitoring of vascular dynamics in human fingers, Photoacoustics 23 (2021), 100282, https://doi.org/10.1016/j.pacs.2021.100282.

[16] M.A. Mastanduno, S.S. Gambhir, Quantitative photoacoustic image reconstruction improves accuracy in deep tissue structures, Biomed. Opt. Express 7 (10) (2016) 3811–3825, https://doi.org/10.1364/BOE.7.003811.

[17] J. Zeng, R. Wang, A. Teng, X. Song, Research on photoacoustic effect of picosecond laser pulse with tissue based on finite element method, Proc. SPIE 11844 (2021), 1184416, https://doi.org/10.1117/12.2601380.

[18] S.L. Jacques, Coupling 3D Monte Carlo light transport in optically heterogeneous tissues to photoacoustic signal generation, Photoacoustics 2 (2014) 137–142, https://doi.org/10.1016/j.pacs.2014.09.001.

[19] Y.S. Yuan, S. Yan, Q.Q. Fang, Light transport modeling in highly complex tissues using the implicit mesh-based Monte Carlo algorithm, Biomed. Opt. Express 12 (2021) 147–161, https://doi.org/10.1364/BOE.411898.

[20] V. Periyasamy, M. Pramanik, Advances in monte carlo simulation for light propagation in tissue, IEEE Rev. Biomed. Eng. 10 (2017) 122–135, https://doi.org/10.1109/RBME.2017.2739801.

[21] Y.Q. Tang, J.J. Yao, 3D Monte Carlo simulation of light distribution in mouse brain in quantitative photoacoustic computed tomography, Quant. Imaging Med. Surg. 11 (3) (2021) 1046–1059, https://doi.org/10.21037/qims-20-815.

[22] X. Shu, W.Z. Liu, H.F. Zhang, Monte Carlo investigation on quantifying the retinal pigment epithelium melanin concentration by photoacoustic ophthalmoscopy, J. Biomed. Opt. 20 (10) (2020), 106005, https://doi.org/10.1117/1.JBO.20.10.106005.

[23] A.N. Bashkatov, E.A. Genina, V.V. Tuchin, G.B. Altshuler, I.V. Yaroslavsky, Monte Carlo study of skin optical clearing to enhance light penetration in the tissue: implications for photodynamic therapy of acne vulgaris, Adv. Laser Technol. 2007 (2008), 702209, https://doi.org/10.1117/12.803909.

[24] Y.E. Hajji, E.H.E. Rhaleb, Melanin effect on light beam intensity distribution in skin as a function of wavelength and depth from 200 to 1000 nm using Monte Carlo simulation, J. Quant. Spectrosc. Radiat. Transf. 295 (2023), 108411, https://doi.org/10.1016/j.jqsrt.2022.108411.

[25] T. Maeda, N. Arakawa, M. Takahashi, Monte Carlo simulation of spectral reflectance using a multilayered skin tissue model, Opt. Rev. 17 (2010) 223–229, https://doi.org/10.1007/s10043-010-0040-5.

[26] B.E. Treeby, B.T. Cox, k-Wave: MATLAB toolbox for the simulation and reconstruction of photoacoustic wave fields, J. Biomed. Opt. 15 (2) (2010), 021314, https://doi.org/10.1117/1.3360308.

[27] X.L. Song, G.Y. Chen, A.J. Zhao, X.Y. Liu, J.H. Zeng, Virtual optical-resolution photoacoustic microscopy using the k-Wave method, Appl. Opt. 60 (2021) 11241–11246, https://doi.org/10.1364/AO.444106.

[28] A. Sharma, M. Pramanik, Convolutional neural network for resolution enhancement and noise reduction in acoustic resolution photoacoustic microscopy, Biomed. Opt. Express 11 (2020) 6826–6839, https://doi.org/10.1364/BOE.411257.

[29] N. Akhlaghi, T.J. Pfefer, K.A. Wear, B.S. Garra, W.C. Vogt, Multidomain computational modeling of photoacoustic imaging: verification, validation, and image quality prediction, Jr. Biom. Opt. 24 (12) (2019), 121910, https://doi.org/10.1117/1.JBO.24.12.121910.

[30] M. Heijblom, D. Piras, E. Maartens, E.J.J. Huisman, F.M. van den Engh, J. M. Klaase, W. Steenbergen, S. Manohar, Appearance of breast cysts in planar geometry photoacoustic mammography using 1064-nm excitation, 126009-126009, J. Biomed. Opt. 18 (12) (2013), https://doi.org/10.1117/1.JBO.18.12.126009.

[31] P. Valeriya, K. Daria, K. Aleksandr, K. Mikhail, Combined Monte Carlo and k-wave simulations for reconstruction of blood oxygen saturation in optoacoustics: a pilot study, J. Biomed. Photonics Eng. 8 (4) (2022) 40511, https://doi.org/10.18287/JBPE22.08.040511.

[32] B.A. Kaplan, J. Buchmann, S. Prohaska, J. Laufer, Monte-Carlo-based inversion scheme for 3D quantitative photoacoustic tomography. Photons Ultrasound.: Imaging Sens. 10064 (2017) 802–814, https://doi.org/10.1117/12.2251945.

[33] T. Feng, Y.X. Ge, Y.J. Xie, W.Y. Xie, C.C. Liu, L. Li, D. Ta, Q. Jiang, Q. Cheng, Detection of collagen by multi-wavelength photoacoustic analysis as a biomarker for bone health assessment, Photoacoustics 24 (2021), 100296, https://doi.org/10.1016/j.pacs.2021.100296.

[34] B. Park, C.H. Bang, C. Lee, J.H. Han, W. Choi, J. Kim, G.S. Park, J.W. Rhie, J.H. Lee, C. Kim, 3D wide-field multispectral photoacoustic imaging of human melanomas in vivo: a pilot study, J. Eur. Acad. Dermatol. Venereol. 35 (2021) 669–676, https://doi.org/10.1111/jdv.16985.

[35] N. Cao, Y.H. Li, R.Y. Zhang, S.B. Liu, Y.P. Xiong, H. Cao, Theoretical analysis of photoacoustic effects in a multilayered skin tissue model, AIP Adv. 13 (3) (2023), 035007, https://doi.org/10.1063/5.0136208.

[36] I.R.M. Barnard, P. Tierney, C.L. Campbell, L. McMillan, H. Moseley, E. Eadie, C.T. A. Brown, K. Wood, Quantifying direct DNA damage in the basal layer of skin exposed to UV radiation from sunbeds, Photochem. Photobiol. 94 (2018) 1017–1025, https://doi.org/10.1111/php.12935.

[37] A.E. Karsten, J.E. Smit, Modeling and verification of melanin concentration on human skin type, Photochem. Photobiol. 88 (2012) 469–474, https://doi.org/10.1111/j.1751-1097.2011.01044.x.

[38] T. Lister, P.A. Wright, P.H. Chappell, Optical properties of human skin, J. Biomed. Opt. 17 (2012) 0909011, https://doi.org/10.1117/1.JBO.17.9.090901.

[39] G. Tetteh, V. Efremov, N.D. Forkert, M. Schneider, J. Kirschke, B. Weber, Deepvesselnet: vessel segmentation, centerline prediction, and bifurcation detection in 3d angiographic volumes, Front. Neurosci. 14 (2020), https://doi.org/10.3389/fnins.2020.592352.

[40] I.V. Meglinski, S.J. Matcher, Quantitative assessment of skin layers absorption and skin reflectance spectra simulation in the visible and near-infrared spectral regions, Physiol. Meas. 23 (2002) 741–753, https://doi.org/10.1088/0967-3334/23/4/312.

[41] M. Sand, T. Gambichler, G. Moussa, F.G. Bechara, D. Sand, P. Altmeyer, K. Hoffmann, Evaluation of the epidermal refractive index measured by optical coherence tomography, Ski. Res. Technol. 12 (2006) 114–118, https://doi.org/10.1111/j.0909-752X.2006.00144.x.

[42] G. Altshuler, M. Smirnov, I. Yaroslavsky, Lattice of optical islets: a novel treatment modality in photomedicine, J. Phys. D: Appl. Phys. 38 (2005) 2732–2747, https://doi.org/10.1088/0022-3727/38/15/027.

[43] I.V. Meglinskii, A.N. Bashkatov, E.A. Genina, D. Yu. Churmakov, V.V. Tuchin, Study of the possibility of increasing the probing depth by the method of reflection confocal microscopy upon immersion clearing of nearsurface human skin layers, Quantum Electron. 32 (2002) 875–882, https://doi.org/10.1070/QE2002v032n10ABEH002309.

[44] R.C. Smith, K.S. Baker, Optical properties of the clearest natural waters (200–800 nm), Appl. Opt. 20 (1981) 177–184, https://doi.org/10.1364/AO.20.000177.

[45] K.F. Palmer, D. Williams, Optical properties of water in the near infrared, J. Opt. Soc. Am. A 64 (1974) 1107–1110, https://doi.org/10.1364/JOSA.64.001107.

[46] S.L. Jacques, Optical properties of biological tissues: a review, Phys. Med. Biol. 58 (2013) 5007, https://doi.org/10.1088/0031-9155/58/14/5007.

[47] D. Marti, R.N. Aasbjerg, P.E. Andersen, A.K. Hansen, MCmatlab: an open-source, user-friendly, MATLAB-integrated three-dimensional Monte Carlo light transport solver with heat diffusion and tissue damage, J. Biomed. Opt. 23 (12) (2018), 121622, https://doi.org/10.1117/1.JBO.23.12.121622.

[48] D.K. Yao, C. Zhang, K.I. Maslov, L.V. Wang, Photoacoustic measurement of the Grüneisen parameter of tissue, Jr. Biom. Opt. 19 (1) (2014), 017007, https://doi.org/10.1117/1.JBO.19.1.017007.

[49] B.E. Treeby, B.T. Cox, Modeling power law absorption and dispersion for acoustic propagation using the fractional Laplacian, J. Acoust. Soc. Am. 127 (5) (2010) 2741–2748, https://doi.org/10.1121/1.3377056.

[50] K.K. Shung, R.A. Sigelmann, J.M. Reid, Scattering of ultrasound by blood, IEEE Trans. Biomed. Eng. 6 (1976) 460–467, https://doi.org/10.1109/TBME.1976.324604.

[51] O. Ronneberger, P. Fischer, T. Brox, U-Net: convolutional networks for biomedical image segmentation, Proc. Int. Conf. Med. Image Comput. Comput. Assist. Interv. 9351 (2015) 234–241, https://doi.org/10.1007/978-3-319-24574-4_28.

[52] K. Maslov, H. Zhang, S. Hu, L.V. Wang, Optical-resolution photoacoustic microscopy for in vivo imaging of single capillaries, Opt. Lett. 33 (2008) 929–931, https://doi.org/10.1364/OL.33.000929.

[53] L.V. Wang, Multiscale photoacoustic microscopy and computed tomography, Nat. Photon 3 (2009) 503–509, https://doi.org/10.1038/nphoton.2009.157.

[54] B. Park, Reflection-mode switchable subwavelength Bessel-beam and Gaussian-beam photoacoustic microscopy in vivo, J. Biophotonics 12 (2019), e201800215, https://doi.org/10.1002/jbio.201800215.
[55] B. Jiang, X. Yang, Q. Luo, Reflection-mode Bessel-beam photoacoustic microscopy for in vivo imaging of cerebral capillaries, Opt. Express 24 (2016) 20167–20176, https://doi.org/10.1364/OE.24.020167.
[56] E.M. Strohm, E.S. Berndl, M.C. Kolios, High frequency labelfree photoacoustic microscopy of single cells, Photoacoustics 1 (3–4) (2013) 49–53, https://doi.org/10.1016/j.pacs.2013.08.003.
[57] M. Schwarz, D. Soliman, M. Omar, A. Buehler, S.V. Ovsepian, J. Aguirre, V. Ntziachristos, Optoacoustic dermoscopy of the human skin: tuning excitation energy for optimal detection bandwidth with fast and deep imaging in vivo, IEEE Tr. Med. Imag. 36 (6) (2017) 1287–1296, https://doi.org/10.1109/TMI.2017.2664142.
[58] T. Feng, Y. j Xie, W.Y. Xie, Y.N. Chen, P. Wang, L. Li, J. Han, D. Ta, L.M. Cheng, Q. Cheng, Characterization of multi-biomarkers for bone health assessment based on photoacoustic physicochemical analysis method, Photoacoustics 25 (2022), 100320, https://doi.org/10.1016/j.pacs.2021.100320.
[59] E.M.A. Anas, H.K. Zhang, J. Kang, E. Boctor, Enabling fast and high quality LED photoacoustic imaging: a recurrent neural networks based approach, Biomed. Opt. Express 9 (8) (2018) 3852–3866, https://doi.org/10.1364/BOE.9.003852.
[60] P. Farnia, E. Najafzadeh, A. Hariri, S.N. Lavasani, B. Makkiabadi, A. Ahmadian, J. V. Jokerst, Dictionary learning technique enhances signal in LED-based photoacoustic imaging, Biomed. Opt. Express 11 (5) (2020) 2533–2547, https://doi.org/10.1364/BOE.387364.
[61] A. Hariri, K. Alipour, Y. Mantri, J.P. Schulze, J.V. Jokerst, Deep learning improves contrast in low-fluence photoacoustic imaging, Biomed. Opt. Express 11 (6) (2020) 3360–3373, https://doi.org/10.1364/BOE.395683.
[62] S. Guan, A.A. Khan, S. Sikdar, P.V. Chitnis, Fully dense unet for 2-D sparse photoacoustic tomography artifact removal, IEEE J. Biomed. Health Inform. 24 (2) (2020) 568–576, https://doi.org/10.1109/JBHI.2019.2912935.
[63] C.C. Yang, H.R. Lan, F. Gao, F. Gao, Review of deep learning for photoacoustic imaging, Photoacoustics 21 (2021), 100215, https://doi.org/10.1016/j.pacs.2020.100215.
[64] Z.L. Wu, I. Kang, Y.D. Yao, Y. Jiang, J.J. Deng, J. Klug, S. Vogt, G. Barbastathis, Three-dimensional nanoscale reduced-angle ptycho-tomographic imaging with deep learning (RAPID), eLight 3 (2023) 7, https://doi.org/10.1186/s43593-022-00037-9.
[65] C. Zuo, J.M. Qian, S.J. Feng, W. Yin, Y.X. Li, P.F. Fan, J. Han, K.M. Qian, Q. Chen, Deep learning in optical metrology: a review, Light Sci. Appl. 11 (2022) 39, https://doi.org/10.1038/s41377-022-00714-x.
[66] Y. Fan, J.J. Li, L.P. Lu, J.S. Sun, Y. Hu, J.L. Zhang, Z.S. Li, Q. Shen, B.W. Wang, R. N. Zhang, Q. Chen, C. Zuo, Smart computational light microscopes (SCLMs) of smart computational imaging laboratory (SCILab), PhotoniX 2 (2021) 19, https://doi.org/10.1186/s43074-021-00040-2.
[67] J.M. Qian, Y. Cao, Y. Bi, H.J. Wu, Y.T. Liu, Q. Chen, C. Zuo, Structured illumination microscopy based on principal component analysis, eLight 3 (2023) 4, https://doi.org/10.1186/s43593-022-00035-x.

Yang Gao is a master student from Nanjing University of Science and Technology. He is now in the third year of his master's degree and his current research focuses on applications of photoacoustic imaging in biomedicine.

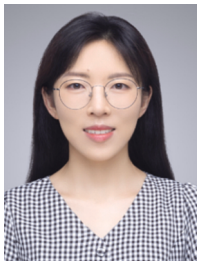

Ting Feng received her bachelor's degree, master's degree and Ph.D. degree from Nanjing University in 2010, 2012 and 2016, respectively. She is currently working at Fudan university in China. She was the visiting scholar at the University of Michigan in 2018 and 2019, and she was the joint-Ph.D. student at the University of Michigan in 2013–2015. Her current research interest includes photoacoustic imaging and measurements. A major part of her research is clinical application of photoacoustic techniques for bone health assessment.

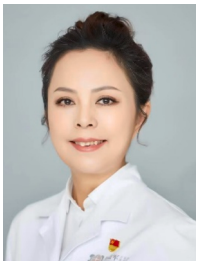

Haixia Qiu is the director of the First Medical Center Laser medicine Department, deputy chief physician, master tutor. Good at strong laser treatment of pigment, vascular and proliferative diseases, fatigue marks, etc. She is currently the executive editorial Board member of the Chinese Journal of Laser Medicine, the Standing Committee member of the Laser Medicine Branch of the Beijing Medical Association, the member of the board of directors of the Chinese Optical Society, and national natural science evaluation expert.

Ying Gu is an academician of the Chinese Academy of Sciences, chief physician, professor, director of Laser Medicine Department of the First Medical Center of PLA General Hospital, Director of Laser Medicine Center of Hainan Hospital. Permanent member of the International Federation of Laser Medicine, Chairman of the Chinese Medical Association Laser Medicine Branch, chairman of the Chinese Optical Society. She presided over the development of China's first laser medicine clinical technology operating standards and diagnosis and treatment guidelines.

Qian Chen as a leading expert in the National Key Discipline of "Optical Engineering" at Nanjing University of Science and Technology. As the primary contributor, he has won a second-class State Technological Invention Award, a second-class State Scientific and Technological Progress Award and five first-class provincial and ministerial-level science and technology awards. As the first inventor, he has obtained 74 granted invention patents, 16 PCT international patents, and 6 U.S. patents. He has authored three books and 374 SCI papers, among which 27 have been featured on the cover. Currently, he serves as a Fellow and Executive Director of the Chinese Society of Optical Engineering and Executive Director of the Chinese Institute of Electronics.

Chao Zuo is a professor in optical engineering, Nanjing University of Science and Technology (NJUST), China. He leads the Smart Computational Imaging Laboratory (SCILab: www.scilaboratory.com) at the School of Electronic and Optical Engineering, NJUST. He has long been engaged in the development of novel Computational Optical Imaging and Measurement technologies, with a focus on Phase Measuring Imaging Metrology such as Holographic Interferometric Microscopy, Noninterferometic Quantitative Phase Imaging (QPI), Fringe Projection Profilometry (FPP), and Structured Illumination Microscopy (SIM). He has authored > 200 peer-reviewed publications in prestigious journals with over 11,000 citations.

Haigang Ma is a associate Professor, Nanjing University of Science and Technology. In the past five years, he has published more than 20 SCI papers on photoacoustic imaging systems, detection methods and application research. Meanwhile, actively participated in promoting the instrumenting of photoacoustic imaging technology, applied for 25 national invention patents in China, and developed the first photoacoustic microscopic imaging instrument applied to clinical skin detection in China , and obtained the registeration certificate for medical device of the People' s Republic of China.